Multi-physics approach to model the lymph transport in the murine immune system

D. S. Grebennikov[abc], B. D. Pivovarov[ad], R. S. Savinkov[abe], G I. Lobov[f], and G. A. Bocharov[*abe]

Abstract — We formulate a compartmental model of the murine lymphatic system with the transfer rate parameters derived from the data on the geometric characteristics of the lymphatic system (LS) graph structure and the Hagen–Poiseuille-based values of the lymph flows through the system components, i.e., vertices and edges. It is supplemented by the physics-based model of lymph node draining-related function which considers a paradigmatic view of its geometry with one- and three-afferent lymphatic vessels and one efferent vessel, and the lymph flow described by the Darcy–Starling equations. We discuss further modelling work needed to gain a predictive understanding of the LS function in response to various perturbations including infections and therapeutic treatments.

The development of computational models that describe the spatiotemporal dynamics of physical, chemical and biological processes in the immune system represents a frontier of the field of mathematical immunology [1]. The spatial structure of the immune system and its transport processes are contingent upon the network- and hydrodynamic characteristics of the lymphatic system (LS) and lymphoid organs. Previously, we constructed a network-type model of the LS of mice specified in the form of an oriented graph [4]. To this end, the Hagen–Poiseuille equations were employed in order to describe the stationary lymph flow balance within the LS. A further step in modelling the functioning lymphatic system implies the transition from a mass balance view to a dynamical characterization of the lymph flow through the system.

Lymph nodes (LNs) are major structural and functional units of the immune

[a]Marchuk Institute of Numerical Mathematics, Russian Academy of Sciences, Moscow 119333
* E-mail: g.bocharov@inm.ras.ru

[b]Moscow Center for Fundamental and Applied Mathematics at INM RAS

[c]World-Class Research Center 'Digital biodesign and personalized healthcare', Sechenov First Moscow State Medical University, Moscow 119991

[d]Sechenov First Moscow State Medical University, Moscow 119991

[e]Institute for Computer Science and Mathematical Modelling, Sechenov First Moscow State Medical University, Moscow 119991

[f]Pavlov Institute of Physiology, Russian Academy of Sciences, Saint-Petersburg 199034

system. They play a key role in the perfusion of lymph through the LS [2, 8]. Until now, the models of lymph dynamics in human and murine LS have ignored the pumping and reservoir function of LNs [13, 14]. The overall efforts on integrative modelling of the structure and function of the whole lymphatic system still remain rather limited [9, 12].

The primary aim of this study is to formulate a compartmental model of the murine lymphatic system with the transfer rate parameters estimated from the data on the geometric characteristics of the LS structure and the Hagen–Poiseuille-based values of the lymph flows through the system components. In addition, we implement the physics-based model of LN draining-related function considering the paradigmatic view of its geometry with one- and three-afferent lymphatic vessels. The prototypes of the corresponding model are those based on the Darcy–Starling equations with one inlet and one outlet vessel [2, 8, 16]. By comparing the estimate of the pressure drop through the LN treated as a passive chamber in the compartmental model with the pressure required to perfuse the lymph through a physiologically-structured LN, we conclude whether LN-generated pumping needs to be considered in physics-based models of lymph flow in the LS.

In Section 1 we formulate, calibrate and validate the compartmental model of the murine LS. Section 2 presents computational models of the LN with a varying numbers of afferent vessels. Finally, in Section 3 we discuss further modelling work needed to gain a predictive understanding of the LS function in response to various perturbations.

## 1. Compartmental view of the murine lymphatic system

1.1. Compartmental systems

A compartmental system consists of a finite number of macroscopic compartments that interact by exchanging material [6]. Each compartment contains a material which is well mixed and spatially homogeneous. The graph representation of the murine LS as compartmental system with circles standing for the LNs, connectors and drained tissues/organs and the arrows representing the transfer of material (lymph) into or out of compartments is shown in Fig. 1. The graph $G(V, E)$ consists of 89 vertices of which 52 vertices are the peripheral ones and 88 edges.

Following the theory of compartmental systems notation [6], the fractional transfer coefficients or transfer rates represent the fraction of material transferred per unit of time between the respective compartments. Let N be the number of compartments, t be the time, and $Q_i(t)$ be the total material (lymph) in compartment i, $i = 1, \ldots, N$ at time t. The general governing equations for the compartmental dynamics of mass are as follows [7]:

$$\frac{\mathrm{d}Q_i(t)}{\mathrm{d}t} = \sum_{j \neq i} \mu_{ij} Q_j(t) - \sum_{j \neq i} \mu_{ji} Q_i(t) - \mu_{0i} Q_i(t) + I_i(t). \qquad (1.1)$$

Here, μ_{ij}, μ_{0i}, and $I_i(t)$ denote the mass transfer rates from compartment j to i, the mass outflow from compartment i to external environment, and the inflow from
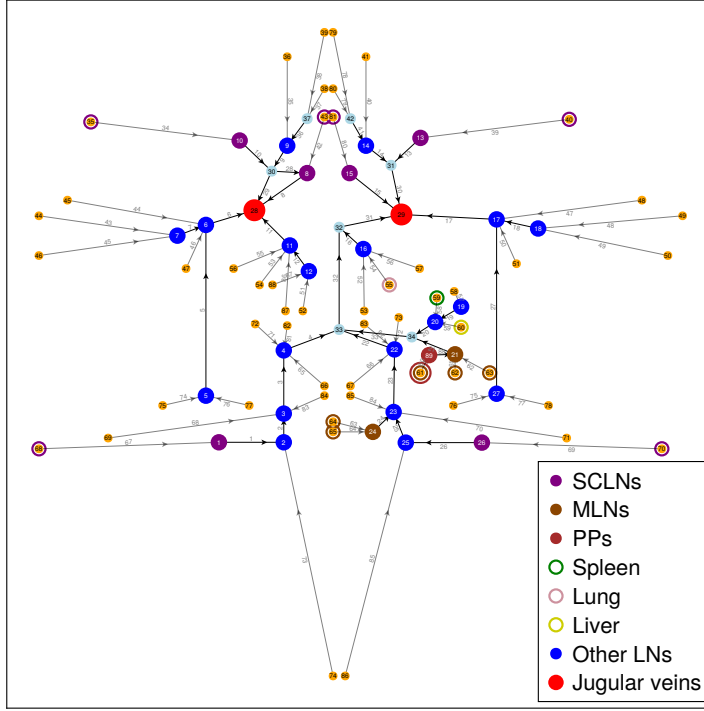
Figure 1. The oriented graph of the murine LS (modified from [4]) illustrating the connections between the compartments (89 vertices) in the compartmental system (equation 1.1) with the arrows (88 oriented edges) indicating the transport orientation. Four types of compartments are shown: (1) tissues or organs from which the lymph is initially collected (orange vertices), (2) lymph nodes categorized into subcutaneous LNs (SCLNs, purple), mesentric LNs (MLNs, light brown), Peyer's patches (PPs, brown) and other lymph nodes (blue), (3) jugular veins to which the lymph is finally delivered from the periphery (red), (4) connectors, i.e., fusion points of multiple lymphatic vessels (cyan). The compartments representing the organs (left lung, spleen, liver) in which the recirculation of labelled lymphocytes in rats was analyzed in [5] (apart from the blood, SCLNs, MLNs and PPs) are encircled with colours indicated in the legend. The transport from the generalized blood compartment (which includes the jugular veins) to the organs and the transport from the individual lymph nodes directly to the blood compartment are not shown to prevent cluttering the figure.

external environment to compartment i, respectively. If the transfer coefficients are constant or depend only on time, the respective system is called a linear compartmental system. We consider a linear compartmental model to describe lymphatic flow in the murine LS. For a qualitative validation of the calibrated model the following properties can be used. If we rewrite the linear version of the system (1.1) in a matrix-vector form

$$\frac{\mathrm{d}\mathbf{Q}(t)}{\mathrm{d}t} = \mathbf{F}\mathbf{Q}(t) + \mathbf{I}(t) \tag{1.2}$$

where $\mathbf{Q} = [Q_1, Q_2, \ldots, Q_N]^T$, then the elements of the transfer coefficient matrix

$\mathbf{F} = [f_{ij}]_{i,j=1}^N$ have the following three properties (see [7]):

$$f_{ii} \leqslant 0; \qquad f_{ij} \geqslant 0, \quad i \neq j; \qquad \sum_i f_{ij} \leqslant 0. \tag{1.3}$$

These properties follow from the mass conservation principle taking into account the non-negativity of parameters in (1.1) and the definition the matrix $\mathbf{F}$ elements (see [7] for details): $f_{ji} = \mu_{ji}$, $f_{ii} = -\mu_{0i} - \sum_{j \neq i} \mu_{ji}$.

The initial value problem for the system of ODEs (1.1) with corresponding initial conditions specified in the following section was solved numerically using the package DifferentialEquations.jl [18].

1.2. Model calibration

To estimate the transfer rates μ_{ji} of the linear version of the compartmental system (1.2) from the stationary lymph flow in the LS graph (see Fig. 1), we used the following relationship for the bulk flow rate q_{ji} and velocity v_{ji} through the vessel (i.e., the edge connecting the vertices i to j) with length l_{ji} and the radius r_{ji}:

$$v_{ji} = \frac{q_{ji}}{\pi r_{ji}^2} \tag{1.4}$$

$$\mu_{ji} = \frac{v_{ji}}{l_{ji}} \tag{1.5}$$

where the flow rates q_{ji} were computed according to the Hagen–Poiseuille law-based model as previously described [4].

Lymph flow rates, and hence, the transfer rates of the compartmental model were estimated according to the following three scenarios:

(1) all the radii of the vessels $r_{j,i}$ are equal to 150 μm;

(2) the radius of the thoracic duct is 300 μm, the radius of the most distant vessel is equal to 41 μm, and the radii of the vessels from the jugular veins to the peripheral vertices decrease linearly with the distance;

(3) the sum of the cross-sectional areas of the vessels is equal to the sum of the input vessels, and the radii of all the vessels adjacent to the peripheral vertices are considered equal and calculated so that the radius of the thoracic duct is 300 μm.

The estimates of the velocities v_{ji} and transfer coefficients μ_{ji} for the three scenarios of the vessel radii r_{ji} are summarized in Fig. 2. To visualize the transfer coefficients for the three scenarios, an adjacency matrix is shown in Fig. 3, which provides a global pattern-type view of the respective systemic transfer coefficients.

The numerical values of the transfer coefficients of the compartmental model of the murine LS are summarized in Table 1 using the notation $\mu_{j,i}$.
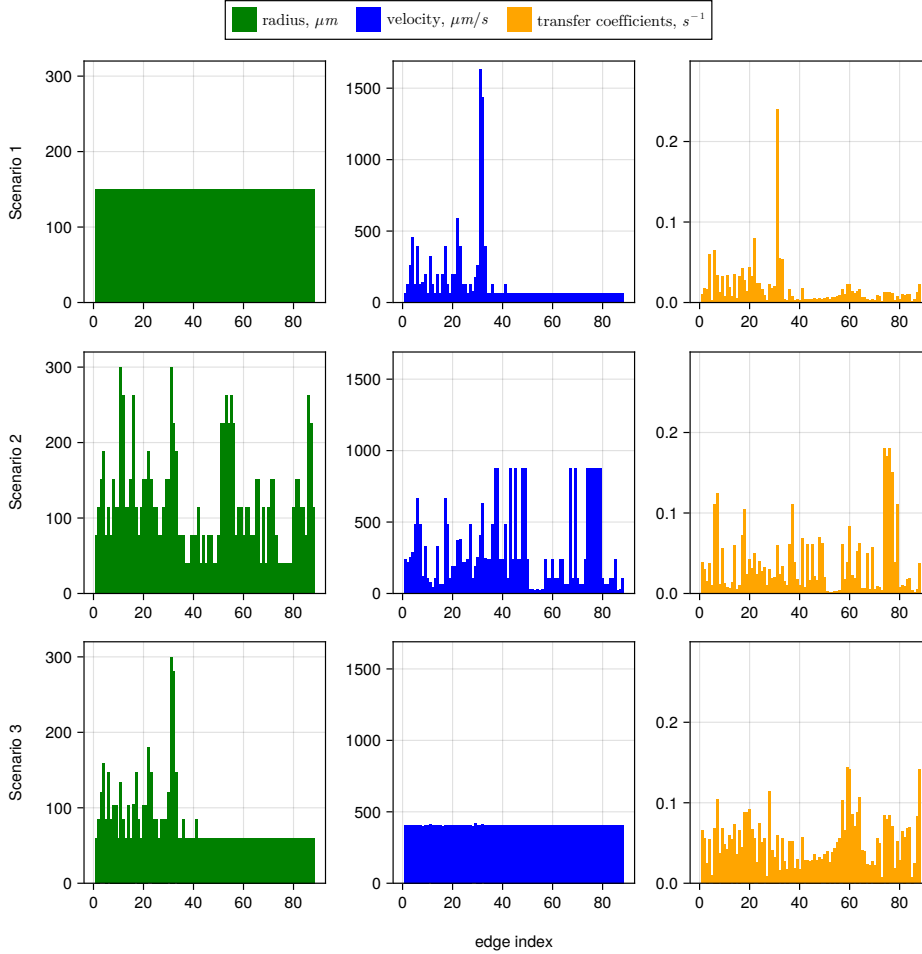
Figure 2. The distribution of radii (left), flow velocities (center) and transfer rates (right) for the murine LS appearing in equations (1.4) and (1.5) computed according to the Hagen–Poiseuille law-based model [4]. The edges are enumerated by the indices as labelled in Fig. 1.

1.3. Model validation

The overall set of parameters meets the formal definition of the transfer coefficient matrix specified by equations (1.3). We used the data on recirculation kinetics of lymphocytes from rats [15] to specify the reference values for early kinetics of the mass transfer in the LS. The numerical simulation of the early mass kinetics and the corresponding experimental data from [15] are shown in Fig. 4. It appears that Scenario 1 is more consistent with the data than the other two.

In [3], a compartmental model was considered to describe the lymphocyte recirculation between the following compartments: organs (left lung, liver, spleen), groups of LNs, i.e., subcutaneous (SCLNs), mesenteric (MLNs), Peyers patches

Table 1. Estimated transfer coefficients (s^{-1}).

Coeff.	Scenario 1	Scenario 2	Scenario 3	Coeff.	Scenario 1	Scenario 2	Scenario 3
$\mu_{2,1}$	1.0×10^{-2}	3.9×10^{-2}	6.5×10^{-2}	$\mu_{3,2}$	1.8×10^{-2}	3.0×10^{-2}	5.6×10^{-2}
$\mu_{4,3}$	1.6×10^{-2}	1.6×10^{-2}	2.5×10^{-2}	$\mu_{33,4}$	6.1×10^{-2}	3.8×10^{-2}	5.4×10^{-2}
$\mu_{6,5}$	3.0×10^{-3}	1.1×10^{-2}	9.3×10^{-3}	$\mu_{28,6}$	6.6×10^{-2}	1.1×10^{-1}	6.8×10^{-2}
$\mu_{6,7}$	3.4×10^{-2}	1.2×10^{-1}	1.0×10^{-1}	$\mu_{28,8}$	1.4×10^{-2}	1.2×10^{-2}	3.7×10^{-2}
$\mu_{30,9}$	3.3×10^{-2}	5.6×10^{-2}	6.9×10^{-2}	$\mu_{30,10}$	7.8×10^{-3}	1.3×10^{-2}	4.9×10^{-2}
$\mu_{28,11}$	3.4×10^{-2}	8.5×10^{-3}	4.3×10^{-2}	$\mu_{11,12}$	1.9×10^{-2}	6.2×10^{-3}	6.0×10^{-2}
$\mu_{31,13}$	8.7×10^{-3}	1.5×10^{-2}	5.4×10^{-2}	$\mu_{31,14}$	3.5×10^{-2}	6.0×10^{-2}	7.4×10^{-2}
$\mu_{29,15}$	5.7×10^{-3}	5.5×10^{-3}	3.5×10^{-2}	$\mu_{32,16}$	3.2×10^{-2}	1.1×10^{-2}	6.6×10^{-2}
$\mu_{29,17}$	4.2×10^{-2}	7.2×10^{-2}	4.4×10^{-2}	$\mu_{17,18}$	2.8×10^{-2}	1.0×10^{-1}	8.8×10^{-2}
$\mu_{20,19}$	1.4×10^{-2}	2.4×10^{-2}	8.8×10^{-2}	$\mu_{34,20}$	4.4×10^{-2}	4.3×10^{-2}	9.2×10^{-2}
$\mu_{34,21}$	3.2×10^{-2}	3.2×10^{-2}	6.7×10^{-2}	$\mu_{33,22}$	8.0×10^{-2}	5.0×10^{-2}	5.6×10^{-2}
$\mu_{22,23}$	2.5×10^{-2}	2.4×10^{-2}	2.6×10^{-2}	$\mu_{23,24}$	2.4×10^{-2}	4.1×10^{-2}	7.5×10^{-2}
$\mu_{23,25}$	1.7×10^{-2}	2.8×10^{-2}	5.2×10^{-2}	$\mu_{25,26}$	8.9×10^{-3}	3.3×10^{-2}	5.6×10^{-2}
$\mu_{17,27}$	2.9×10^{-3}	1.1×10^{-2}	9.1×10^{-3}	$\mu_{8,30}$	2.3×10^{-2}	3.1×10^{-2}	1.1×10^{-1}
$\mu_{28,30}$	1.8×10^{-2}	1.9×10^{-2}	4.1×10^{-2}	$\mu_{29,31}$	2.1×10^{-2}	2.0×10^{-2}	3.2×10^{-2}
$\mu_{29,32}$	2.4×10^{-1}	6.0×10^{-2}	6.0×10^{-2}	$\mu_{32,33}$	5.5×10^{-2}	2.4×10^{-2}	1.6×10^{-2}
$\mu_{33,34}$	5.4×10^{-2}	3.4×10^{-2}	5.6×10^{-2}	$\mu_{10,35}$	4.3×10^{-3}	1.6×10^{-2}	2.7×10^{-2}
$\mu_{9,36}$	2.8×10^{-3}	1.0×10^{-2}	1.7×10^{-2}	$\mu_{9,37}$	1.7×10^{-2}	6.1×10^{-2}	5.2×10^{-2}
$\mu_{37,38}$	8.3×10^{-3}	1.1×10^{-1}	5.2×10^{-2}	$\mu_{37,39}$	3.0×10^{-3}	4.0×10^{-2}	1.8×10^{-2}
$\mu_{13,40}$	4.8×10^{-3}	1.8×10^{-2}	3.0×10^{-2}	$\mu_{14,41}$	2.9×10^{-3}	1.1×10^{-2}	1.8×10^{-2}
$\mu_{14,42}$	1.9×10^{-2}	6.8×10^{-2}	5.8×10^{-2}	$\mu_{8,43}$	4.5×10^{-3}	7.7×10^{-3}	2.8×10^{-2}
$\mu_{7,44}$	4.6×10^{-3}	6.1×10^{-2}	2.9×10^{-2}	$\mu_{6,45}$	4.4×10^{-3}	1.6×10^{-2}	2.8×10^{-2}
$\mu_{7,46}$	4.6×10^{-3}	6.1×10^{-2}	2.9×10^{-2}	$\mu_{6,47}$	5.8×10^{-3}	2.1×10^{-2}	3.6×10^{-2}
$\mu_{17,48}$	4.6×10^{-3}	1.7×10^{-2}	2.9×10^{-2}	$\mu_{18,49}$	5.2×10^{-3}	7.0×10^{-2}	3.3×10^{-2}
$\mu_{18,50}$	4.7×10^{-3}	6.3×10^{-2}	2.9×10^{-2}	$\mu_{17,51}$	5.7×10^{-3}	2.1×10^{-2}	3.6×10^{-2}
$\mu_{12,52}$	6.4×10^{-3}	2.8×10^{-3}	4.0×10^{-2}	$\mu_{16,53}$	4.1×10^{-3}	1.8×10^{-3}	2.6×10^{-2}
$\mu_{11,54}$	6.2×10^{-3}	2.0×10^{-3}	3.9×10^{-2}	$\mu_{16,55}$	6.9×10^{-3}	3.0×10^{-3}	4.3×10^{-2}
$\mu_{11,56}$	8.2×10^{-3}	2.7×10^{-3}	5.1×10^{-2}	$\mu_{16,57}$	8.9×10^{-3}	3.9×10^{-3}	5.6×10^{-2}
$\mu_{19,58}$	1.6×10^{-2}	6.1×10^{-2}	1.0×10^{-1}	$\mu_{20,59}$	1.1×10^{-2}	1.8×10^{-2}	6.6×10^{-2}
$\mu_{20,60}$	2.3×10^{-2}	3.9×10^{-2}	1.4×10^{-1}	$\mu_{89,61}$	2.3×10^{-2}	8.3×10^{-2}	1.4×10^{-1}
$\mu_{21,62}$	1.4×10^{-2}	2.3×10^{-2}	8.6×10^{-2}	$\mu_{21,63}$	1.1×10^{-2}	1.9×10^{-2}	7.1×10^{-2}
$\mu_{24,64}$	1.4×10^{-2}	5.2×10^{-2}	8.9×10^{-2}	$\mu_{24,65}$	1.7×10^{-2}	6.3×10^{-2}	1.1×10^{-1}
$\mu_{4,66}$	6.6×10^{-3}	6.4×10^{-3}	4.1×10^{-2}	$\mu_{22,67}$	6.4×10^{-3}	6.2×10^{-3}	4.0×10^{-2}
$\mu_{1,68}$	3.8×10^{-3}	5.0×10^{-2}	2.4×10^{-2}	$\mu_{3,69}$	3.6×10^{-3}	6.2×10^{-3}	2.3×10^{-2}
$\mu_{26,70}$	4.3×10^{-3}	5.8×10^{-2}	2.7×10^{-2}	$\mu_{23,71}$	3.6×10^{-3}	6.1×10^{-3}	2.3×10^{-2}
$\mu_{4,72}$	9.0×10^{-3}	8.8×10^{-3}	5.6×10^{-2}	$\mu_{22,73}$	8.0×10^{-3}	7.8×10^{-3}	5.0×10^{-2}
$\mu_{2,74}$	1.3×10^{-3}	4.7×10^{-3}	7.9×10^{-3}	$\mu_{5,75}$	1.3×10^{-2}	1.8×10^{-1}	8.4×10^{-2}
$\mu_{27,76}$	1.3×10^{-2}	1.7×10^{-1}	8.0×10^{-2}	$\mu_{5,77}$	1.3×10^{-2}	1.8×10^{-1}	8.4×10^{-2}
$\mu_{27,78}$	1.1×10^{-2}	1.5×10^{-1}	7.0×10^{-2}	$\mu_{42,79}$	3.0×10^{-3}	4.0×10^{-2}	1.8×10^{-2}
$\mu_{42,80}$	8.3×10^{-3}	1.1×10^{-1}	5.2×10^{-2}	$\mu_{15,81}$	4.5×10^{-3}	7.6×10^{-3}	2.8×10^{-2}
$\mu_{4,82}$	1.0×10^{-2}	1.0×10^{-2}	6.5×10^{-2}	$\mu_{22,83}$	9.2×10^{-3}	9.0×10^{-3}	5.7×10^{-2}
$\mu_{3,84}$	1.1×10^{-2}	1.8×10^{-2}	6.8×10^{-2}	$\mu_{23,85}$	1.1×10^{-2}	1.9×10^{-2}	6.9×10^{-2}
$\mu_{25,86}$	1.3×10^{-3}	4.7×10^{-3}	7.9×10^{-3}	$\mu_{11,87}$	3.9×10^{-3}	1.3×10^{-3}	2.4×10^{-2}
$\mu_{12,88}$	1.3×10^{-2}	5.8×10^{-3}	8.3×10^{-2}	$\mu_{21,89}$	2.3×10^{-2}	3.8×10^{-2}	1.4×10^{-1}

(PPs), blood and a generalized compartment of the other and tissues in the rest of the body. We have used the estimates of transfer rates from [3] to estimate the rates of transfer between the blood and the input vertices of the graph which represent a particular organ or which represent the tissues drained by a particular group of LNs. The indices of the vertices (column 2 in Table 2) which represent the compartments considered in [3], as well as the indices of the input vertices of our graph-

Table 2. Estimated transfer rates between the blood compartment, organs and lymph nodes. The blood compartment is denoted as b. (The data from [3] are used.)

Organ	Vertices, k	Collecting vertices, l	Entrance from blood, $\mu_{b,l}$ (s^{-1})	Exit from organ into blood, $\mu_{k,b}$ (s^{-1})
Left lung	55 ($n_K = 1$)	55 ($n_L = 1$)	3×10^{-2}	3.6×10^{-2}
Liver	60 ($n_K = 1$)	60 ($n_L = 1$)	6.8×10^{-3}	2.8×10^{-3}
Spleen	19 ($n_K = 1$)	19 ($n_L = 1$)	9.3×10^{-4}	1.1×10^{-4}
SCLNs	8, 15, 10, 13, 1, 26 ($n_K = 6$)	35, 40, 43, 81, 68, 70 ($n_L = 6$)	6.9×10^{-5}	9.4×10^{-6}
MLNs	21, 24 ($n_K = 2$)	64, 65, 62, 63 ($n_L = 4$)	2.2×10^{-5}	2.8×10^{-5}
PPs	89 ($n_K = 1$)	61 ($n_L = 1$)	8.8×10^{-5}	5.6×10^{-5}
Other LNs	$n_K = 19$	$n_L = 38$	2.5×10^{-6}	3.2×10^{-3}

based compartmental model (collecting vertices, column 3) standing for the tissues which are drained by these lymph nodes, are presented in Table 2. The rate of entrance into the collecting vertices from the blood compartment $\mu_{b,l}$ was estimated as $\mu_{b,l} = \mu_{\text{blood,organ}}/n_L$, where $\mu_{\text{blood,organ}}$ is the estimate from [3] and n_L is the number of the collecting vertices for the considered organ. The rates of transfer from the vertices representing the organs to the blood were estimated as $\mu_{k,b} = \mu_{\text{organ,blood}}/n_K$, where $\mu_{\text{organ,blood}}$ is the estimate from [3] and n_K is the number of the vertices representing the considered organ.

Table 2 lists the resulting generalized estimates of the transfer coefficients. Figure 5 summarizes our data and data from [3] as a graph-type diagram of the murine compartmental system with the estimated transfer rates for Scenario 1, including the transfer rates between the graph vertices and the blood (output compartments). The transfer rates between the indicated compartments (vertices) and blood were estimated by data from Table 2, whereas the transfer rates for vessels (edges) presented according to Table 1.

### 1.4. Homeostatic distribution of the substance across various compartments

We used the compartmental model to predict the kinetics of mass distribution following some standard routes of injections via temporal vein or subcutaneous mode. These predictions are relevant for planning pharmacokinetic studies of drug distribution as well as in studies of experimental virus infections.

Firstly, the kinetics of mass appearance in the right and left jugular veins (vertices 28, 29, respectively) following intravenous (temporal vein) injection is presented in Fig. 6. The model predicts about two-fold difference in the amount of substance transferred to the left and to the right jugular vein for all three scenarios, with the slower rate for Scenario 1 and the fastest rate for Scenario 3.

Secondly, the distribution of the substance in Scenario 1 after injection into the vertex 68, corresponding to subcutaneous injection administered into the right hind limb and the subsequent transfer of the substance to the jugular vein, is shown in Fig. 7. The predicted kinetics characterizes a relative presence of the injected substance in respective parts of the LS following subcutaneous introduction. It transiently accumulates in popliteal-, external sacral- and iliac nodes over the first 500 seconds and finally, leaves the LS in about 1000 seconds.
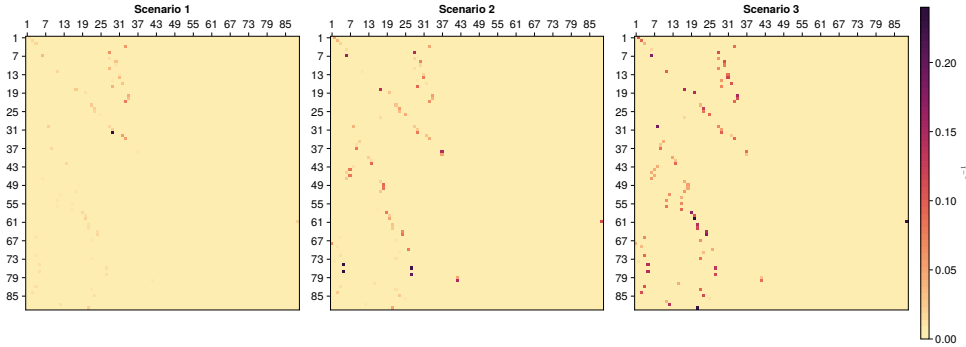
Figure 3. Adjacency matrix for the compartmental model of the murine lymphatic system with the elements standing transfer rates (s^{-1}) corresponding to three scenarios of the lymphatic vessel diameter changes from the inlet to outlet compartments.
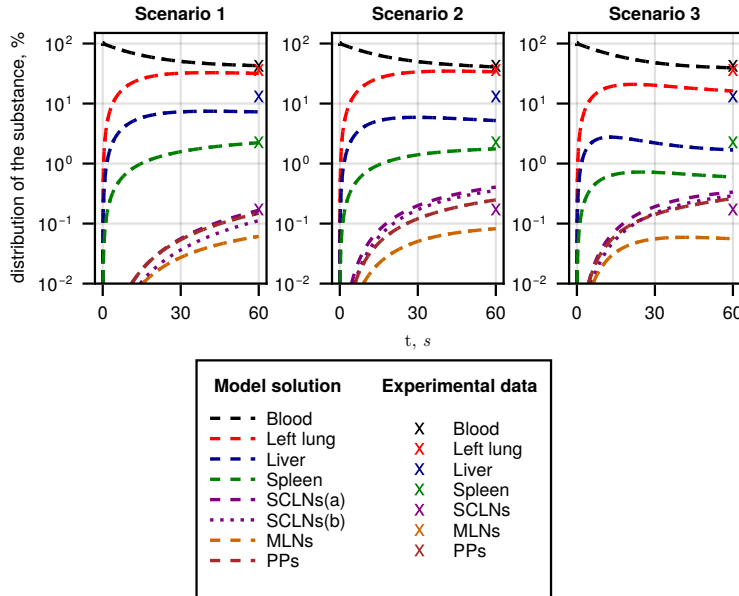
Figure 4. Early mass kinetics predicted by the compartmental model of the murine LS. The experimental data from [15] are marked by symbols. The group of subcutaneous lymph nodes (SCLNs) defined in [15] consists of popliteal (vertices 1, 26), deep cervical (vertices 8, 15) and superficial cervical (see below) lymph nodes. Due to the difference in nomenclature of murine LNs in [15] and [4], we considered two options of mapping superficial cervical LNs on the LS graph: as vertices 10, 13, which corresponds to the dashed curves SCLNs (a), or as vertices 9-10, 13-14, which corresponds to the dotted curves SCLNs (b).

Finally, Figure 8 shows the stationary mass distribution in the LS time for three scenarios under assumption that the system is closed. Assuming the substance is transferred from the blood to the LS compartments at a rate of 0.038 s^{-1} [3], we have set the transfer rate from the blood to each peripheral compartment to $0.038/n \text{ s}^{-1}$,
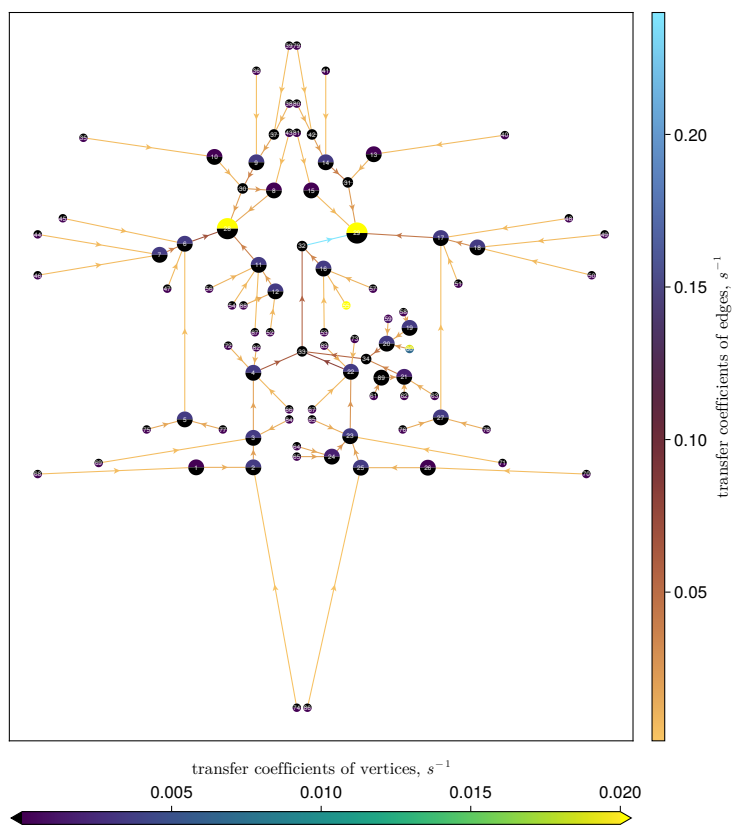
Figure 5. Visualization of the transfer coefficients (s^{-1}) on graph of the murine LS according to Scenario 1. In the vertices, the colour at the top means the rate of exit from the vertex into the blood, the colour at the bottom — entrance into the vertex from the blood.

where $n = 52$ is the number of input vertices.

One can conclude that the homeostatic distribution of the substance in the LS of mice under the assumption of no connection to external environment (closed system) strongly depends on the scenario of the evolution of the radii of the lymphatic vessels from the inlet to outlet compartments. For example, the vertices 32–33, corresponding to the thoracic duct, appear to be the most substance accumulating compartments in Scenario 2 and 3. In Scenario 1, the substance distribution looks more uniform across the LS than in other two scenarios. In Scenario 2, the model predicts a larger accumulation of the mass in the lung and surrounding LNs.

2. Model of lymph flow through LN

The compartmental model considers LN as a passive chamber. However, it allows us to estimate a scale of the pressure drop between the incoming and outcoming vessels according to Hagen–Poiseuille equation. By comparing it to the pressure
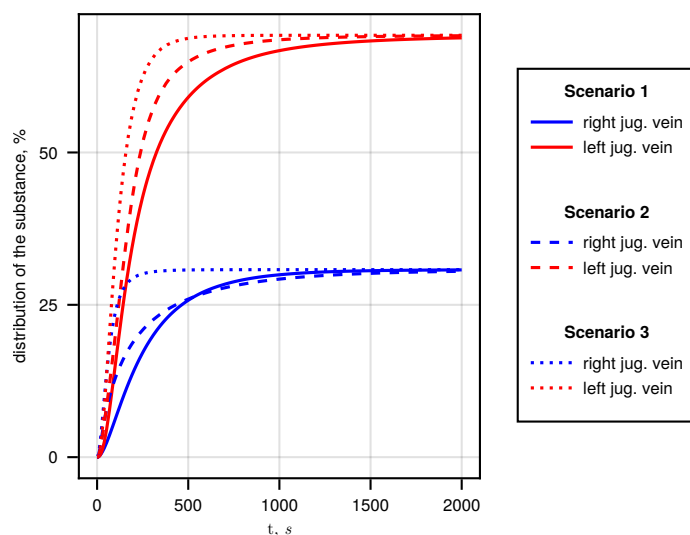
Figure 6. The kinetics of relative mass transfer to the right and left jugular veins (vertices 28, 29, respectively) for initial values in the peripheral vertices taken as $100\%/n$, where $n = 52$ is the number of peripheral vertices. This scenario corresponds to intravenous injection into temporal vein.
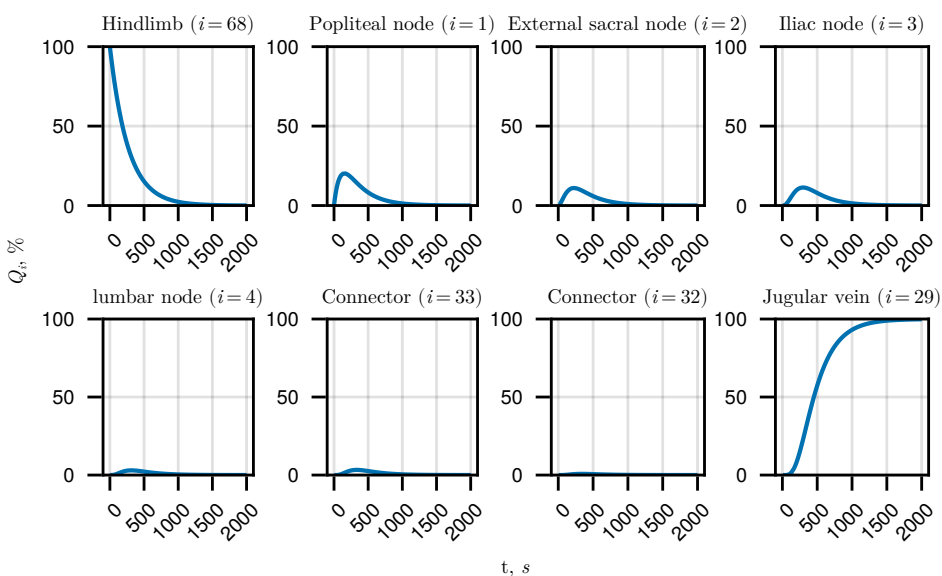
Figure 7. The distribution kinetics of the substance in Scenario 1 after injection into the vertex 68, corresponding to subcutaneous injection administered into the right hind limb, and the subsequent transfer of the substance to the jugular vein.

required for lymph filtration through the LN when its spatial and biomechanical characteristics are considered, we could conclude whether an active contraction of
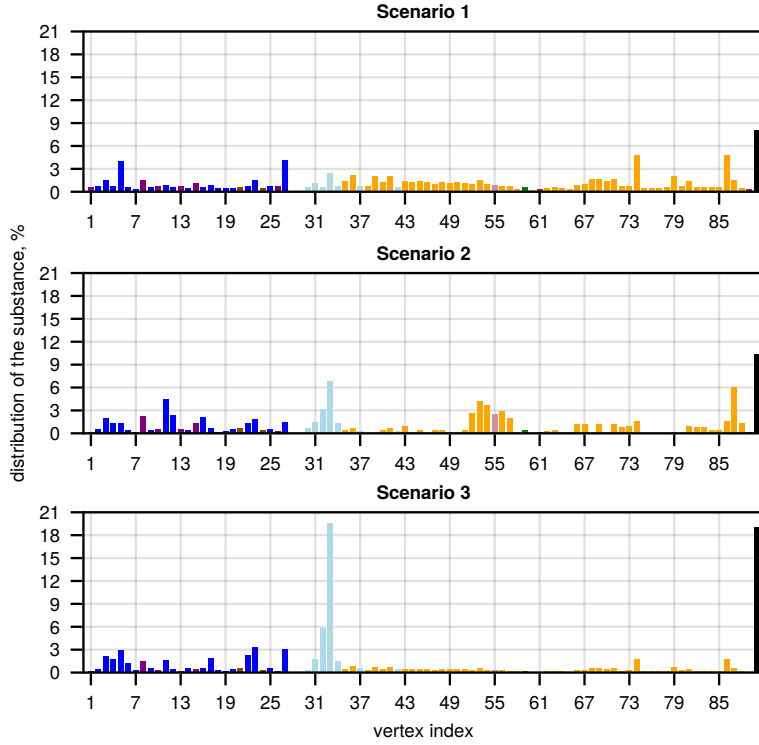
Figure 8. Stationary distribution of the substance in the murine lymphatic system according to the compartmental model under the assumption of no influx and outflux from the system ODEs integrated up to $t = 10^5$ seconds. The vertices are marked by their type using the same colour notation as in Fig. 1. The output vertices 28–29 (right and left jugular veins) have been connected to the extra vertex 90 representing the blood compartment (black) with instantaneous transfer between them. The vertices are enumerated by the indices as labelled in Fig. 1.

LNs is needed for a normal function of LS under physiological conditions. To this end, we use the Darcy–Starling equations for modelling the lymph flow in LN under homeostatic conditions.

Transfer of lymph through the lymph nodes is essential for maintaining the fluid balance between the tissues and the blood vascular system and for the functioning of the immune system. We consider the following simplified geometrical model of a murine lymph node: (a) the domain of the lymph node $\Omega = \Omega_{SS} \cup \Omega_C \cup \Omega_A \cup \Omega_E$ consists of the outer and inner subdomains representing the subcapsular sinus (Ω_{SS}) and the cortex (Ω_C), as well as the slight cylindrical extensions from the capsule of the lymph node representing the interfaces with the afferent and efferent lymphatic vessels (Ω_A and Ω_E), (b) the capsule $\Gamma_{cap} = \partial \Omega_{SS}$ is represented by an ellipsoid with the lengths of semi-axes $r_x = 500$, $r_y = 300$, $r_z = 300$ μm, (c) the boundary of the cortex area $\partial \Omega_C$ is represented by a concentric ellipsoid with the lengths of semi-axes being h_{SS} smaller than that of the capsule, where $h_{SS} = 10$ μm is the width
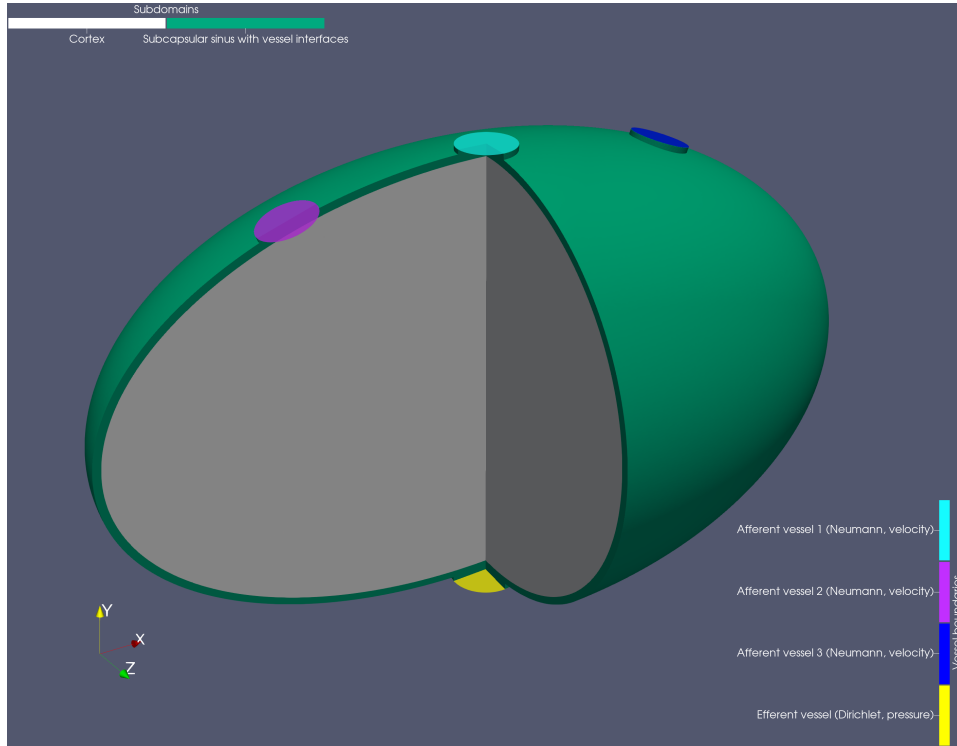
Figure 9. The geometry of the computational domain for a lymph node with three afferent vessels, illustrating (1) the boundaries Γ_A^i, $i \in \{1,2,3\}$ with Neumann condition for the afferent inflow velocity (cyan, magenta and blue), (2) the boundary Γ_E with Dirichlet condition for the efferent pressure (yellow), as well as (3) the cortex area Ω_C (white) and the area of the rest of domain $\Omega \setminus \Omega_C$ (green). A quarter of the lymph node is clipped to show the interior subdomains.

of the subcapsular sinus, (d) the single efferent lymphatic vessel interface Ω_E is a cylinder with diameter $r_E = 100 \, \mu m$ located at the lower pole of the lymph node that extends orthogonally to the Γ_{cap} on $h_{SS}/2$, (e) the afferent lymphatic vessel interface Ω_A consists of one to four similar cylinders Ω_A^i with diameters $r_A = 75 \, \mu m$ located at the upper side of the lymph node, i.e., at the opposite side from the efferent vessel. The outer boundaries of the vessel interfaces cross-sectional to the axes of cylinders Ω_A^i and Ω_E are denoted as Γ_A^i and Γ_E. The computational domain is illustrated in Fig. 9 for a lymph node with three afferent vessels.

The lymph flow through the lymph nodes is considered to be subject to the Darcy law of flow in porous media and the volume continuity equation for lymph velocity $\boldsymbol{v}(\boldsymbol{x})$ and pressure $p(\boldsymbol{x})$:

$$\boldsymbol{v}(\boldsymbol{x}) = -\frac{K_{SS}}{\mu} \nabla p(\boldsymbol{x}), \quad \nabla \cdot \boldsymbol{v}(\boldsymbol{x}) = 0, \quad \boldsymbol{x} \in \Omega \setminus \Omega_C$$

$$\boldsymbol{v}(\boldsymbol{x}) = -\frac{K_C}{\mu} \nabla p(\boldsymbol{x}), \quad \nabla \cdot \boldsymbol{v}(\boldsymbol{x}) = -q_s(\boldsymbol{x}), \quad \boldsymbol{x} \in \Omega_C \tag{2.1}$$

$$q_s(\boldsymbol{x}) = k_f((p(\boldsymbol{x}) - p_{BV}) - \sigma \Delta \pi), \quad \boldsymbol{x} \in \Omega_C$$

where permeability in the cortex area (K_C) is much lower than in the rest of domain (K_{SS}), μ is the dynamic viscosity of lymph, and $q_s(\boldsymbol{x})$ is the sink term applied in the cortex area Ω_C, which represents the volume flux absorbed from the lymph node into the blood vessels and capillaries (which are assumed to permeate the cortex homogeneously according to the Starling equation) with the filtration coefficient k_f, the average difference in oncotic pressure between blood and lymph $\Delta\pi = \pi_{BV} - \pi_{\text{lymph}}$, the reflection coefficient σ, and with the average blood pressure p_{BV}.

System (2.1) is subject to boundary conditions

$$
\begin{aligned}
\boldsymbol{n}(\boldsymbol{x}) \cdot \boldsymbol{v}(\boldsymbol{x}) &= 0, \quad \boldsymbol{x} \in \partial\Omega \setminus \Gamma_A \setminus \Gamma_E \\
\boldsymbol{n}(\boldsymbol{x}) \cdot \boldsymbol{v}(\boldsymbol{x}) &= -v_A, \quad \boldsymbol{x} \in \Gamma_A \\
p(\boldsymbol{x}) &= p_E, \quad \boldsymbol{x} \in \Gamma_E
\end{aligned}
\tag{2.2}
$$

where Γ_A and Γ_E represent the outer boundaries of the afferent and efferent vessel interfaces cross-sectional to the cylinders, $\boldsymbol{n}(\boldsymbol{x})$ is the outer unit normal vector, v_A is the velocity magnitude of the lymph inflow through Γ_A, and p_E is the pressure at Γ_E.

System (2.1)–(2.2) is solved numerically using the finite volume method with the two-point-flux approximation scheme in Dumux package [19]. The underlying unstructured conformal tetrahedral mesh refined towards the vessel interfaces and the subcapsular sinus was constructed using Gmsh [20].

The following parameter estimates have been used taking into account the previous modelling studies [2, 4, 8, 16]: $K_C = 2.8 \cdot 10^{-4}$ μm^2, $K_{SS} = 1.5$ μm^2, $\mu = 0.0015$ Pa·s, $p_{BV} = 5$ mmHg, $\sigma = 0.88$, $\Delta\pi = 7.7$ mmHg, $k_f = 770$ (Pa·s)$^{-1}$, $v_A = 10$ mm/min ≈ 167 μm/s, $p_E = 2.5$ mmHg, rescaled to SI units.
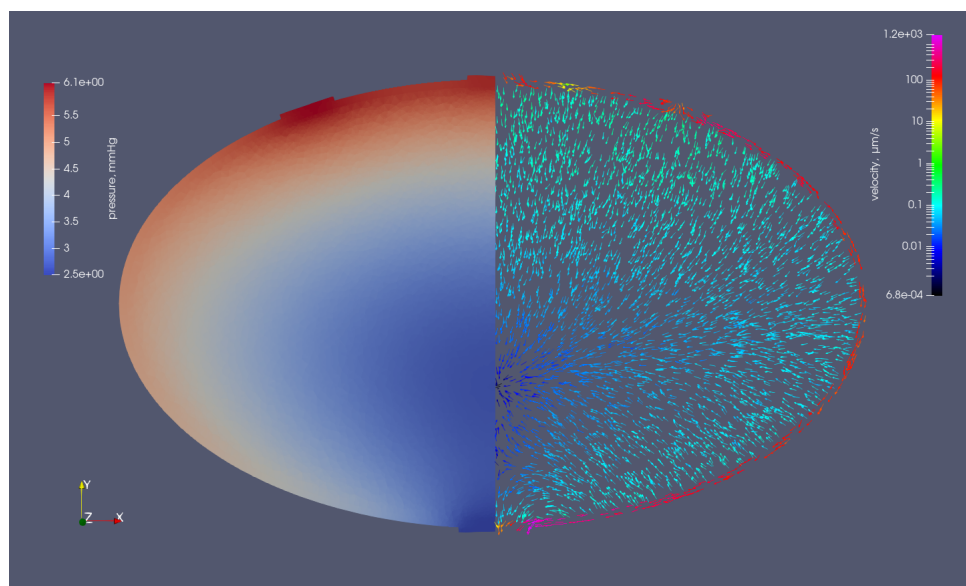
The resulting lymph flow in the cross section of the lymph node with one afferent vessel is shown in Fig. 10. The velocity profile demonstrates the values from 10 to 230 μm/s in the subcapsular sinus, while the filtration through the densely packed cortex is much slower, with velocities less than 1 μm/s. One can see that the pressure at the afferent vessel (which will be denoted as p_A) is larger than the pressure at the efferent one, while at the center of the cortex, where the lymph is absorbed into the blood, the pressure is lower than p_E. The pressure drop from the efferent vessel to the cortex center is greater than the difference in pressure between the efferent and afferent vessels $p_A - p_E$. The 5-fold decrease in filtration coefficient k_f results in a different pressure distribution (Fig. 11) with $p_A - p_E$ much larger than the pressure drop towards the cortex center. In the lymph node with three afferent vessels (Fig. 12), with the same parameters as in Fig. 10, the lymph inflow from three afferent vessels creates a larger pressure gradient between the afferent and efferent vessels (about 3 mmHg versus 0.5 mmHg in the case of LN with a single afferent vessel). The pressure is higher in the lateral afferent vessels rather than in the central one. The pressure at the cortex center is not lower than pressure at the efferent vessel, in contrast to the previous scenarios with a single afferent vessel, but there is still an apparent absorption of lymph into the blood. The maximum velocity magnitude in subcapsular sinus increases 10-fold, up to 1200 μm/s ≈ 72 mm/min near the sink into the efferent vessel.
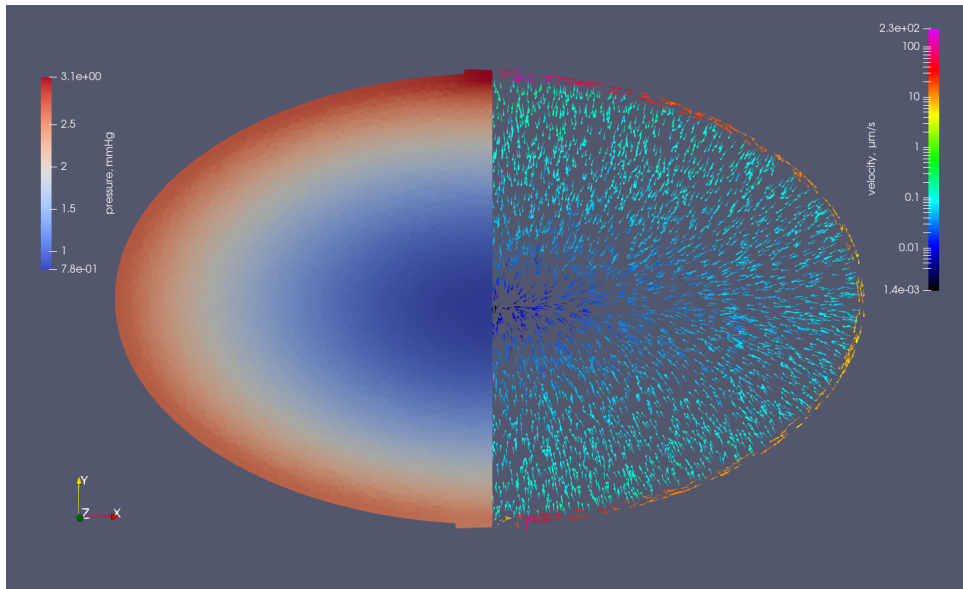
Figure 10. The lymph flow in the cross-section of the lymph node with a single afferent vessel. Left part presents the distribution of pressure, while the right part shows the velocity field. The parameters are as indicated in the text.
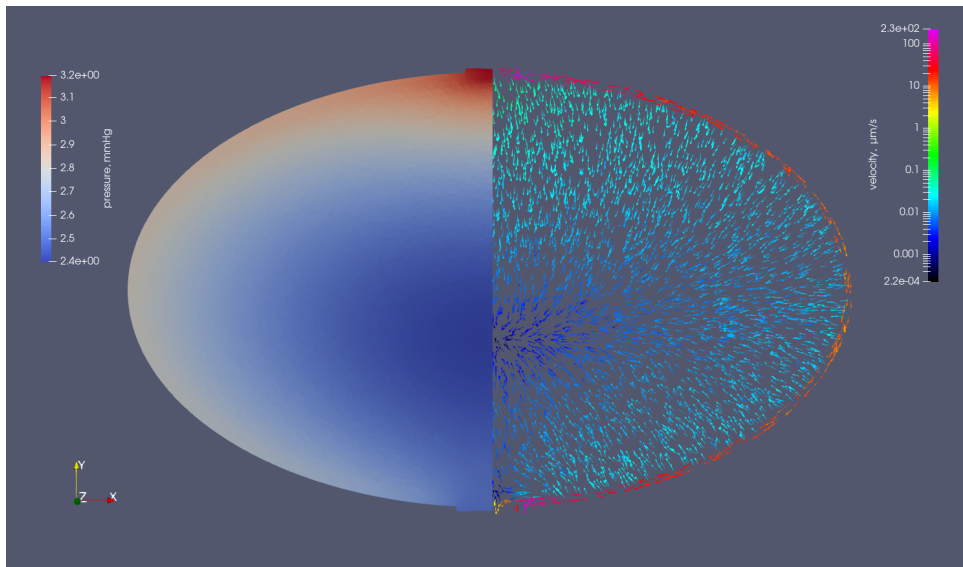
Figure 11. The lymph flow in the cross-section of the lymph node with a single afferent vessel. Left part presents the distribution of pressure, while the right part shows the velocity field. The parameters are as indicated in the text except for the filtration coefficient k_f which is decreased 5-fold.

Figure 12. The lymph flow in the cross-section of the lymph node with three afferent vessels. Left part presents the distribution of pressure, while the right part shows the velocity field. The parameters are as indicated in the text.

The pressure drop required for supporting the estimated inflow and outflow of lymph flow through the LN predicted by the compartment model is about 1 mmHg. The pressure needed for lymph flow through the LN predicted by the physics-based model is much larger, i.e., about 4 mmHg. The about 4-fold difference suggests that active contractions of the LN and/or afferent vessels are required to ensure the lymph flow through the LN.

3. Discussion

In our study, we developed a comprehensive compartmental model of the murine LS. It can be used in experimental studies for predicting the pharmacokinetics of drugs and low-weight molecular substances. Additionally, we explored the Darcy–Starling based model of lymph flow through the LN. It served to answer the basic question of LS physiology whether active contractions of LNs and lymphatic vessels are required for normal drainage function of the LS [17]. The analysis predicts that the lymphatic pumping seems to be critically needed.

The application of compartmental analysis to the modelling of particular biological systems is considered in terms of three major problems: (i) the formulation of the compartmental model, (ii) the analytical treatment and (iii) the inverse problem [6]. The latter is the most difficult, as it requires solid data sets to be obtained experimentally [5]. In our study, we explored a different approach to model calibration, i.e., to use an anatomical and physics-based model [4] to estimate the transfer rates of the compartmental models of the murine LS.

The limitation of the presented approach is related to considering a passive nature of lymph flow through the system (ignoring the active contraction of the lymphangions [11] and LNs) and the differences in the kinetics of the substance distribution, which depend on the biological properties of the injected substances. It is possible to distinguish three major types of transported objects:

(1) low molecular weight substances that enter the tissues/organs and the lymph, i.e., they mix throughout the body and reach a steady state (if we ignore the degradation of molecules), as we can see when we take an estimate of the transfer rates from the calculated lymph flows;

(2) high molecular weight substances (> 10–100 kDa) will mostly remain in the blood. They do not directly enter the lymphatic system (unless they are viral particles that are captured by antigen-presenting cells to be delivered to the draining LNs), or special molecules covered with the lipophilic shell;

(3) lymphocytes, for which it is necessary to evaluate the transfer coefficients based on experimental data, rather than using estimates from calculations of the lymph flow through the lymphatic vessels and into the LNs, since their transport is not only a passive process with the lymph flow but involves a number of other factors.

We have developed two key elements for modelling the structure and function of the LS, i.e., the systemic compartmental model (global description) and the physics-based model of the LN with a varying number of afferent lymphatic vessels (local description). The LN model will be integrated into the global LS model to replace the static LN-representing compartments.

To reproduce the properties of LNs in terms of their influence on the lymph flow in the lymphatic system, the future work will be based on the use of trained artificial neural networks (ANNs) as follows. With information on flows and pressures on the afferent vessels of the LNs as input data, the flow and pressure at the beginning of the efferent vessel can be calculated using a neural network model. The neural network (NN) could be of a multi-layer perceptron type. The NN-type model topology implies one or more layers of neurons, which should allow us to adapt the behaviour of the network to reproduce the dependence of pressure and lymph flow from the LN in relation to the input parameters as shown in our previous study [16]. The integration of the NN-based model and the systemic model of lymphatic flow in the murine LS will provide a powerful computational tool for predictive understanding of the immune system function in response to various perturbations of its homeostasis ranging from pathogens to combination immunomodulatory treatments.

References

1. G. A. Bocharov, D. S. Grebennikov, and R. S. Savinkov, Multiphysics modelling of immune processes using distributed parameter systems. *Russian Journal of Numerical Analysis and Mathematical Modelling* **38** (2023), No. 5, 279–292.

2. L. J. Cooper, J. P. Heppell, G. F. Clough, B. Ganapathisubramani, and T. Roose, An image-based model of fluid flow through lymph nodes. *Bull. Math. Biol.* **78** (2016), No. 1, 52–71.

3. V. V. Ganusov and J. Auerbach, Mathematical modeling reveals kinetics of lymphocyte recirculation in the whole organism. *PLoS Comput. Biol.* **10** (2014), No. 5, e1003586.

4. D. Grebennikov, R. Savinkov, E. Zelenova, G. Lobov, and G. Bocharov, Network modeling of murine lymphatic system. *Algorithms* **16** (2023), No. 3, 168.

5. Z. H. Farooqi and R. R. Mohler, Distribution models of recirculating lymphocytes. *IEEE Trans Biomed Eng.* **36** (1989), No. 3, 355–362.

6. J. A. Jacquez, *Compartmental Analysis in Biology and Medicine*, 2nd ed., Ann Arbor, University of Michigan Press, 1985.

7. L. A. Jacquez and C. P. Simon, Qualitative theory of compartmental systems with lags. *Math. Biosci.* **180** (2002), No. 1-2, 329–362.

8. M. Jafarnejad, M. C. Woodruff, D. C. Zawieja, M. C. Carroll, and J. E. Moore, Modeling lymph flow and fluid exchange with blood vessels in lymph nodes. *Lymphat. Res. Biol.* **13** (2015), No. 4, 234–247.

9. T. D. Jayathungage Don, S. Safaei, G. D. Maso Talou, P. S. Russell, A. R. J. Phillips, and H. M. Reynolds, Computational fluid dynamic modeling of the lymphatic system: a review of existing models and future directions. *Biomech. Model. Mechanobiol.* **23** (2024), No. 1, 3–22.

10. K. N. Margaris and R. A. Black, Modelling the lymphatic system: challenges and opportunities. *J. R. Soc. Interface* **9** (2012), No. 69, 601–612.

11. J. E. Moore and C. D. Bertram, Lymphatic system flows. *Annu. Rev. Fluid Mech.* **50** (2018), 459–482.

12. A. Mozokhina and R. Savinkov, Mathematical modelling of the structure and function of the lymphatic system. *Mathematics* **8** (2020), No. 9, 1467.

13. A. S. Mozokhina, S. I. Mukhin, and G. I. Lobov, Pump efficiency of lymphatic vessels: numeric estimation. *Russian Journal of Numerical Analysis and Mathematical Modelling* **34** (2019), No. 5, 261–268.

14. R. Savinkov, D. Grebennikov, D. Puchkova, V. Chereshnev, I. Sazonov, and G. Bocharov, Graph theory for modeling and analysis of the human lymphatic system. *Mathematics* **8** (2020), No. 12, 1–18.

15. M. E. Smith and W. L. Ford, The recirculating lymphocyte pool of the rat: a systematic description of the migratory behaviour of recirculating lymphocytes. *Immunology* **49** (1983), No. 1, 83–94.

16. R. Tretiakova, A. Setukha, R. Savinkov, D. Grebennikov, and G. Bocharov, Mathematical modeling of lymph node drainage function by neural network. *Mathematics* **9** (2021), No. 23, 3093.

17. R. Tretyakova, R. Savinkov, G. Lobov, and G. Bocharov, Developing computational geometry and network graph models of human lymphatic system. *Computation* **6** (2018), No. 1, 1.

18. `https://diffeq.sciml.ai/` [Online; accessed September 6, 2024]

19. `https://dumux.org/` [Online; accessed September 6, 2024]

20. `https://gmsh.info/` [Online; accessed September 6, 2024]